Mathematics

https://www.aimspress.com/journal/Math

AIMS Mathematics, 11(9): 29727–29753.
DOI: 10.3934/math.20261179
Received: 12 May 2026
Revised: 15 August 2026
Accepted: 28 August 2026
Published: 14 September 2026

Research article

Bifurcation and solutions of the fractional order Fokas system using reliable approaches

Asim Alawfi[1] **and M. B. Almatrafi**[2,*]

[1] Department of Mathematics and Statistics, College of Science, Imam Mohammad Ibn Saud Islamic University (IMSIU), Riyadh 11566, Saudi Arabia

[2] Department of Mathematics, College of Science, Taibah University, Al-Madinah Al-Munawarah, Saudi Arabia

* **Correspondence:** Email: mmutrafi@taibahu.edu.sa.

Abstract: This research analyzed the bifurcation structure, stability dynamics, and traveling wave solutions of the nonlinear Fokas system utilizing the D-truncated fractional derivative. Nonlinear pulse transmission in monomode optical fibers was described using the Fokas model. The proposed nonlinear partial differential problem was successfully converted to an ordinary differential equation using a suitable wave transformation. The equilibrium points of the considered model were obtained. The stability and propagation properties of the derived system were shown graphically. In addition, the bifurcation investigation revealed the presence of numerous dynamical domains and critical parameter constraints linked to modifications in the system's qualitative behavior. Some accurate traveling wave solutions were successfully produced by employing a Sardar-subequation method, resulting in a variety of solitary, periodic, and singular wave structures that represented the model's dynamical behavior. Moreover, the qualitative features of the generated solutions were investigated using phase-plane analysis and bifurcation theory. We showed that the reduced amplitude equation, and, hence, its bifurcation structure, does not depend on the fractional orders; the D-truncated operator acted only on the traveling coordinate, rescaling where and when a given profile was realized. Parameter regimes in which each profile was real and bounded were stated explicitly, and only the bounded profiles were interpreted as physically admissible optical pulses.

Keywords: Fokas system; equilibrium points; stability; traveling wave solutions; bifurcation; Sardar-subequation method
Mathematics Subject Classification: 34D05, 34D08, 34D35, 37N25, 37N30, 39A30

1. Introduction

Traveling wave solutions are important in both theoretical and applied sciences because they provide an effective basis for analyzing the propagation process of physical events that retain their form as they move through space and time [1]. For example, traveling wave solutions explain the movement of shallow water waves and internal ocean waves in fluid dynamics. This provides an adequate explanation for the energy transmission and wave stability in natural systems. Traveling wave solutions appear in reaction-diffusion equations to depict the propagation of chemical concentrations, nerve impulses, and epidemic peaks in biological systems [2]. Traveling wave solutions are also employed in nonlinear optics to perfectly illustrate the propagation of optical solitons in fiber cables, which are important for long-distance high-speed communication networks because of the fact that they can preserve shape over time [3]. In addition, these solutions, which appear in solid-state and plasma physics, characterize dislocations and shock waves. Traveling wave solutions are beneficial tools for analyzing real-world phenomena. They also have an ability to simplify complex partial differential problems into simpler ordinary differential equations. Recent work has continued to broaden the analytical methodology for nonlinear evolution equations, including the Painlevé integrability and N-soliton solutions of generalized stochastic Korteweg-de Vries equations [4], and the wave patterns of coupled nonlinear Schrödinger equations in photonic crystal fibers with four-wave mixing [5].

In recent studies, the analysis of the Fokas system with D-truncated derivatives has received considerable amount of attention, especially in relation to fractional calculus and its applications to nonlinear wave equations. According to Mohammed et al. [6], dimensional extensions of the Fokas equation, especially the (4+1)-dimensional form, were constructed by using M-truncated derivatives. Their study concentrates on the mathematical foundation of the time-fractional Fokas equation, emphasizing how fractional temporal behavior is captured by the M-truncated derivative. Some solutions for the stochastic fractional Fokas system with M-truncated derivatives, which include optical solitons and wave structures, were thoroughly investigated in [7]. Al-Askar [8] investigated some solitons for the Fokas-Lenells equation with M-truncated derivatives. Moreover, some soliton solutions of the Fokas wave equations with truncated M-fractional derivatives were established in [9] using novel solution methods. Note that these techniques make it possible to generate explicit solutions that highlight the complex interactions between fractional order effects and nonlinearity. New soliton structures for a (4+1)-dimensional Fokas framework were established in [10]. This study highlighted the possibility of unique optical phenomena in monomode fibers. In order to demonstrate the system's ability to sustain localized wave structures, Rao et al. [11] concentrated on obtaining lump-soliton solutions. Furthermore, numerous solitary waves, bifurcation structures, and chaotic patterns were nicely discovered by Alotaibi et al. [12]. The Kudryashov method was employed by Murad et al. [13] to derive optical soliton solutions for a time-fractional Fokas system, showing the system's flexibility in fractional calculus frameworks. Moreover, the investigation in [14] combined the conformable fractional calculus with the generalized Riccati-Bernoulli-sub-ordinary differential equation approach and Bäcklund transformation to find the pulse propagation in mono-mode optical fibers for the fractional Fokas system. Mohammed et al. [15] utilized the extend F-expansion technique and the Jacobi elliptic function approach to find the traveling wave solutions of system (1.1) in the forms of rational, hyperbolic, elliptic, and trigonometric functions. In general, the published work shows that the Fokas system is a deep and adaptable model that can explain a broad range of nonlinear wave events, from complex chaotic and fractional behaviors to classical solitons, with considerable implications for nonlinear physics and optical fiber technology.

This article is mainly motivated by the increasing utility of nonlinear evolution models in simulating complicated physical events observed in the fields of fluid mechanics, plasma physics, nonlinear optics, and the propagation of waves. Among these models, the Fokas system has received a significant amount of attention due to its complex mathematical structure and extensive practical applicability. Fokas initially presented the Fokas system as an integrable nonlinear evolution equation that emerged in nonlinear wave propagation and mathematical physics [16, 17]. Recently, fractional generalizations of the Fokas system have been developed to represent complicated wave propagation phenomena in media that are characterized with fractional-order behavior and anomalous dispersion. In monomode optical fibers, nonlinear pulse transmission can be explained by the Fokas system [15]. The analytical behavior of the Fokas system under fractional-order operators has received comparatively limited attention, and existing analyses with truncated derivatives have concentrated on the construction of exact solutions. These include M-truncated soliton and wave structures for the (4+1)-dimensional [6] and Fokas-Lenells [8] forms, solutions of the stochastic fractional Fokas system obtained with the aid of bifurcation analysis [7], efficient constructions for truncated M-fractional Fokas wave models [9,10], lump-soliton solutions [11], optical solitons via the Kudryashov approach [13], conformable Riccati-Bernoulli and Bäcklund constructions [14], and F-expansion and Jacobi elliptic function solutions [15]. The present work complements this line by coupling exact traveling-wave solutions with a qualitative dynamical analysis of the reduced system.

The Sardar-subequation profiles obtained in Section 6 are not claimed to be new: Up to reparametrization, they overlap with families already available for the Fokas system through the F-expansion, Jacobi elliptic, Kudryashov, and Riccati-Bernoulli constructions cited above, to which they reduce for $p = q = 1$ and the corresponding choices of (r_0, r_1). What the present study adds is the reading of those profiles through the first integral of the reduced equation: Each profile is assigned to an explicit level set of the conserved Hamiltonian, which fixes its trajectory class and separates the bounded profiles, admissible as optical pulses, from the singular ones. We carry out the associated equilibrium, stability and Hamiltonian bifurcation analysis within the equivariant framework of Golubitsky and Stewart [18], and we record that the reduced bifurcation diagram is independent of the fractional orders δ and β, so that the analysis applies to the full fractional model and not only to its integer-order limit. A symmetry-extended continuation [19, 20] of the symmetry-breaking locus is included as a verification of the equivariant defining system against a case whose answer is known in closed form. The current study demonstrates a direct relationship between the produced traveling-wave solutions and the bifurcation structure of the reduced Hamiltonian system, in contrast to previous studies that mainly concentrated on developing exact analytical solutions. This combined analytical strategy offers a qualitative description of wave forms and clarifies the dynamical principles that underpin their existence. In particular, the main aim of this work is to obtain the traveling wave solutions, equilibrium points, stability, and bifurcation of the Fokas system with D-truncated derivative [15–17]:

$$iD^{\delta,\beta}_{k,t}H + p_1 H_{xx} + p_2 HG = 0, \quad p_3 G_y = p_4(|H|^2)_x, \tag{1.1}$$

where $H(x, y, t)$ and $G(x, y, t)$ are complex functions. Further, p_j, $\forall j$ are constant. $D^{\delta,\beta}_{k,t}$ presents the D-truncated derivative operator for $\delta \in (0, 1]$ and $\beta > 0$. When $\delta = 1$ and $\beta = 0$, the classical Fokas system is obtained:

$$iH_t + p_1 H_{xx} + p_2 HG = 0, \quad p_3 G_y = p_4(|H|^2)_x.$$

This paper is organized as follows. Section 2 presents the concepts of D-truncated derivative while Section 3 summarizes the Sardar-subequation method. In Section 4, we find the transformation of model (1.1) while Section 5 is devoted to analyze the equilibrium points, stability, and the bifurcation. Moreover, Section 6 obtains the traveling wave solutions of model (1.1). Section 7 discusses the main results and Section 8 concludes this work.

2. D-truncated derivative

The D-truncated derivative provides an analytically tractable setting for the fractional Fokas system considered here, since it admits a closed-form relation to the classical derivative and therefore permits the simultaneous construction of exact traveling-wave solutions and the qualitative analysis of the reduced dynamics. The D-truncated derivative is defined as follows.

Definition 2.1. *Let* $f : [0, \infty) \to \mathbb{R}$*. Then,*

$$D^{\delta,\beta}_{k,t} f(t) = \lim_{h\to 0} \frac{f\big(tE_{k,\beta}(ht^{-\delta})\big) - f(t)}{h}, \quad t > 0, \tag{2.1}$$

where

$$E_{k,\beta}(z) = \sum_{j=0}^{k} \frac{z^j}{\Gamma(j\beta + 1)}. \tag{2.2}$$

Properties:

- Linearity:

$$D(\alpha f + \beta g) = \alpha D(f) + \beta D(g).$$

- Power rule:

$$D(t^\nu) = \frac{\nu}{\Gamma(\beta + 1)} t^{\nu-\delta}.$$

- Product rule:

$$D(fg) = fD(g) + g\,D(f).$$

- Relation with classical derivative:

$$D(f)(t) = \frac{t^{1-\delta}}{\Gamma(\beta + 1)} \frac{df}{dt}. \tag{2.3}$$

Remark 2.1. *The truncation index k does not enter Eq* (2.3)*. Expanding Eq* (2.2) *inside Eq* (2.1)*, the term $j = 0$ contributes $f(t)$ and cancels, the term $j = 1$ contributes $h\,t^{-\delta}/\Gamma(\beta + 1)$, and every term with $j \geq 2$ carries a factor h^j and vanishes in the limit $h \to 0$. Hence, $D^{\delta,\beta}_{k,t} f$ is the same operator for every $k \geq 1$, and Eq* (2.3) *holds with no dependence on k. Equation* (2.3) *also shows that $D^{\delta,\beta}_{k,t}$ is a* local *operator: It is a classical derivative weighted by $t^{1-\delta}/\Gamma(\beta + 1)$. This is a property the D-truncated* *derivative shares with the M-truncated, conformable, and β-derivatives employed in the works cited in Section 1, and it has a direct consequence for what follows: Under a traveling-wave ansatz any such operator produces a classical reduced equation. Accordingly, the reduced amplitude equation obtained in Section 4 carries no dependence on k, δ, or β, and we do not claim otherwise. The role that δ and β do play is identified in Section 7: They enter the traveling coordinate, and therefore determine where and when in (x, y, t) a given profile is realized, without altering which profiles exist.*

3. The Sardar-subequation method

In order to explain the Sardar-subequation method, we use the following nonlinear evolution equation (NLE):

$$S(H, G, iD^{\delta,\beta}_{k,t}H, D^{\delta,\beta}_{k,t}G, D^{\delta,\beta}_{k,x}H, D^{\delta,\beta}_{k,x}G, D^{\delta,\beta}_{k,y}H, D^{\delta,\beta}_{k,x,x}H, \ldots) = 0, \tag{3.1}$$

where $H = H(x, y, t)$ and $G = G(x, y, t)$ are unknown functions. Moreover, S is a polynomial in H and G, respectively, and their derivatives. In order to solve Eq (3.1), we use the traveling wave transformation

$$H(x, y, t) = \Phi(\tau)e^{iw}, \quad G(x, y, t) = \Psi(\tau), \tag{3.2}$$

where

$$w = w_1x + w_2y + \frac{w_3\Gamma(\beta + 1)}{\delta}t^{\delta}, \ \ \tau = \tau_1x + \tau_2y + \frac{\tau_3\Gamma(\beta + 1)}{\delta}t^{\delta},$$

where $w_i, \tau_i, \ \forall i$ are constants. The physically relevant solutions meet the asymptotic requirements for localized solitary waves $\Phi(\tau) \longrightarrow 0$ and $\Phi'(\tau) \to 0$ as $|\tau| \to \infty$, whereas periodic solutions satisfy appropriate periodicity conditions. Next, we use Eq (3.2) to convert Eq (3.1) to the following ordinary differential equations:

$$Q(\Phi, \Psi, \Phi', \Psi', \Phi'', \Psi'', \ldots) = 0, \tag{3.3}$$

where $\Phi' = \frac{d\Phi}{d\tau}$, $\Phi'' = \frac{d^2\Phi}{d\tau^2}$, $\Psi' = \frac{d\Psi}{d\tau}$, $\Psi'' = \frac{d^2\Psi}{d\tau^2}$, etc. Under suitable smoothness assumptions on the solution functions, the traveling-wave transformation is still admissible since the D-truncated derivative can be stated using a weighted classical derivative and maintains the chain rule. We then utilize a specific relation between Φ and Ψ to transform Eq (3.3) into the following equation:

$$Q(\Phi, \Phi', \Phi'', \ldots) = 0. \tag{3.4}$$

The Sardar-subequation method gives the solution of Eq (3.4) on the form

$$\Phi(\tau) = \sum_{i=0}^{\rho} \mu_i U^i(\tau). \tag{3.5}$$

Here, μ_i are constants and $\mu_\rho \neq 0$. The value of ρ is obtained by the balance between the nonlinear term and the highest derivative. Note that the function $U(\tau)$ satisfies

$$(U'(\tau))^2 = r_0 + r_1U^2(\tau) + U^4(\tau), \tag{3.6}$$

where r_0 and r_1 are constants.

Case I: If $r_1 > 0$ and $r_0 = 0$, then

$$U_1^{\pm}(\tau) = \pm\sqrt{-pq\,r_1}\,\mathrm{sech}_{pq}(\sqrt{r_1}\,\tau), \quad U_2^{\pm}(\tau) = \pm\sqrt{pq\,r_1}\,\mathrm{csch}_{pq}(\sqrt{r_1}\,\tau),$$

where

$$\mathrm{sech}_{pq}(\tau) = \frac{2}{pe^{\tau} + qe^{-\tau}}, \quad \mathrm{csch}_{pq}(\tau) = \frac{2}{pe^{\tau} - qe^{-\tau}}.$$

Case II: If $r_1 < 0$ and $r_0 = 0$, then

$$U_3^{\pm}(\tau) = \pm\sqrt{-pq\,r_1}\,\sec_{pq}(\sqrt{-r_1}\,\tau), \quad U_4^{\pm}(\tau) = \pm\sqrt{-pq\,r_1}\,\csc_{pq}(\sqrt{-r_1}\,\tau).$$

Case III: If $r_1 < 0$ and $r_0 = \frac{r_1^2}{4}$, then

$$U_5^{\pm}(\tau) = \pm\sqrt{-\frac{r_1}{2}}\,\tanh_{pq}\left(\sqrt{-\frac{r_1}{2}}\tau\right),$$

$$U_6^{\pm}(\tau) = \pm\sqrt{-\frac{r_1}{2}}\,\coth_{pq}\left(\sqrt{-\frac{r_1}{2}}\tau\right),$$

$$U_7^{\pm}(\tau) = \pm\sqrt{-\frac{r_1}{2}}\,\left(\tanh_{pq}\left(\sqrt{-2r_1}\tau\right) \pm i\sqrt{pq}\,sech_{pq}\left(\sqrt{-2r_1}\tau\right)\right),$$

$$U_8^{\pm}(\tau) = \pm\sqrt{-\frac{r_1}{2}}\,\left(\coth_{pq}\left(\sqrt{-2r_1}\tau\right) \pm \sqrt{pq}\,csch_{pq}\left(\sqrt{-2r_1}\tau\right)\right),$$

$$U_9^{\pm}(\tau) = \pm\sqrt{-\frac{r_1}{8}}\,\left(\tanh_{pq}\left(\sqrt{-\frac{r_1}{8}}\tau\right) + coth_{pq}\left(\sqrt{-\frac{r_1}{8}}\tau\right)\right),$$

where

$$\tanh_{pq}(\tau) = \frac{pe^{\tau} - qe^{-\tau}}{pe^{\tau} + qe^{-\tau}}, \quad \coth_{pq}(\tau) = \frac{pe^{\tau} + qe^{-\tau}}{pe^{\tau} - qe^{-\tau}}.$$

Case IV: If $r_1 > 0$ and $r_0 = \frac{r_1^2}{4}$, then

$$U_{10}^{\pm}(\tau) = \pm\sqrt{\frac{r_1}{2}}\,\tan_{pq}\left(\sqrt{\frac{r_1}{2}}\tau\right),$$

$$U_{11}^{\pm}(\tau) = \pm\sqrt{\frac{r_1}{2}}\,\cot_{pq}\left(\sqrt{\frac{r_1}{2}}\tau\right),$$

$$U_{12}^{\pm}(\tau) = \pm\sqrt{\frac{r_1}{2}}\,\left(\tan_{pq}\left(\sqrt{2r_1}\tau\right) \pm \sqrt{pq}\,sec_{pq}\left(\sqrt{2r_1}\tau\right)\right),$$

$$U_{13}^{\pm}(\tau) = \pm\sqrt{\frac{r_1}{2}}\,\left(\cot_{pq}\left(\sqrt{2r_1}\tau\right) \pm \sqrt{pq}\,csc_{pq}\left(\sqrt{2r_1}\tau\right)\right),$$

$$U_{14}^{\pm}(\tau) = \pm\sqrt{\frac{r_1}{8}}\,\left(\tan_{pq}\left(\sqrt{\frac{r_1}{8}}\tau\right) + cot_{pq}\left(\sqrt{\frac{r_1}{8}}\tau\right)\right),$$

where

$$\tan_{pq}(\tau) = -i\frac{pe^{i\tau} - qe^{-i\tau}}{pe^{i\tau} + qe^{-i\tau}}, \quad \cot_{pq}(\tau) = i\frac{pe^{i\tau} + qe^{-i\tau}}{pe^{i\tau} - qe^{-i\tau}}.$$

Next, we find the value of ρ to obtain Eq (3.5). Substituting Eq (3.5) along with Eq (3.6) into Eq (3.4), we end up with an algebraic equation, taking the coefficients of U^j, $\forall j$ to yield a system of equations whose solutions give the values of μ_j, $\forall j$.

4. Transformation of model (1.1)

Now, we insert Eq (3.2) into Eq (1.1) to find the real part which is given by

$$p_1\tau_1^2\Phi'' + (-w_3 - p_1 w_1^2)\Phi + p_2\Phi\Psi = 0, \tag{4.1}$$

$$p_3\tau_2\Psi' = p_4\tau_1(\Phi^2)', \tag{4.2}$$

while the imaginary part is given by

$$(2p_1 w_1\tau_1 + \tau_3)\Phi' = 0. \tag{4.3}$$

Assume that

$$\tau_3 = -2p_1 w_1\tau_1.$$

Integrating Eq (4.2) gives

$$\Psi = \frac{p_4\tau_1}{p_3\tau_2}\,\Phi^2 + C, \tag{4.4}$$

with C an arbitrary constant of integration. Substituting Eq (4.4) into Eq (4.1) and dividing by $p_1\tau_1^2$ yields

$$\Phi'' + a\,\Phi + b\,\Phi^3 = 0, \qquad a = \frac{-w_3 - p_1 w_1^2 + p_2 C}{p_1\tau_1^2}, \qquad b = \frac{p_2 p_4}{p_3 p_1\tau_1\tau_2}, \tag{4.5}$$

so that C shifts the linear coefficient a and leaves the cubic coefficient b, the structure of the equation, and the classification of its equilibria unchanged. Two consequences follow. For the localized profiles, the asymptotic conditions imposed in Section 3 give $\Phi \to 0$ and, hence, $\Psi \to C$ as $|\tau| \to \infty$; requiring the auxiliary field to vanish at infinity forces $C = 0$, so the choice made below is a boundary condition rather than an assumption. For the non-decaying (periodic and singular) profiles, no such condition applies and C remains free; it may then be used to satisfy the balance condition $a = -r_1$ of Section 6 without constraining τ_1. In either case the reduced equation retains the form treated in Section 5, and we set $C = 0$ throughout, which normalizes a. Hence, Eq (4.4) becomes

$$\Psi = \frac{p_4\tau_1}{p_3\tau_2}\Phi^2. \tag{4.6}$$

Substitute Eq (4.6) into Eq (4.1) to obtain

$$\Phi'' + a\Phi + b\Phi^3 = 0, \tag{4.7}$$

where

$$a = \frac{-w_3 - p_1 w_1^2}{p_1\tau_1^2}, \quad b = \frac{p_2 p_4}{p_3 p_1\tau_1\tau_2}. \tag{4.8}$$

5. Bifurcation analysis

The cubic nonlinearity in Eq (4.7) admits multiple equilibrium configurations and supports a symmetry-breaking transition as the control parameter a is varied. Equation (4.7) is the cubic Duffing oscillator, and the equilibrium classification and Hamiltonian pitchfork recalled in this section are classical; they are collected here because they supply the phase-plane vocabulary used in Section 7 to classify the exact profiles, not as new results. To analyze the organization of the solution branches and their stability, we recast Eq (4.7) as a planar first-order system. Setting $z = \Phi$ and $w = \Phi'$, so that $z' = w$ and $w' = \Phi'' = -a\Phi - b\Phi^3 = -az - bz^3$, yields

$$z' = w, \quad w' = -a\,z - b\,z^3, \tag{5.1}$$

which is invariant under the involution $\mathcal{R} : (z, w) \mapsto (-z, -w)$ and admits the conserved Hamiltonian

$$H(z, w) \;=\; \tfrac{1}{2}\,w^2 \;+\; \tfrac{1}{2}\,a\,z^2 \;+\; \tfrac{1}{4}\,b\,z^4. \tag{5.2}$$

The orbits of system (5.1) therefore coincide with the level sets of H, and the bifurcation analysis below can be read either as a local linear analysis of the equilibria or, equivalently, as a topological analysis of the level sets of Eq (5.2). The $\mathbb{Z}_2$ action generated by $\mathcal{R}$ places the problem in the equivariant bifurcation framework of Golubitsky, Stewart, and Schaeffer [18, 21], which we shall use in Subsection 5.4 to organize the two-parameter continuation.

5.1. Equilibria and local stability

The equilibria of Eq (5.1) satisfy

$$w \;=\; 0, \qquad z(a + b\,z^2) \;=\; 0. \tag{5.3}$$

The trivial equilibrium $E_0 = (0, 0)$ exists for all parameter values and lies in the fixed-point subspace of $\mathcal{R}$, while the $\mathcal{R}$-related pair

$$E_\pm \;=\; \left(\pm\sqrt{-a/b},\; 0\right) \tag{5.4}$$

exists if, and only if, $-a/b > 0$. Local stability is governed by the Jacobian

$$J(z, w) \;=\; \begin{pmatrix} 0 & 1 \\ -a - 3bz^2 & 0 \end{pmatrix}. \tag{5.5}$$

At E_0 the characteristic equation reduces to $\lambda^2 + a = 0$, giving $\lambda = \pm\sqrt{-a}$, so E_0 is a (linear) center when $a > 0$ and a saddle when $a < 0$. At $E_\pm$ the Jacobian satisfies $\lambda^2 - 2a = 0$, giving $\lambda = \pm\sqrt{2a}$. The classification of $E_\pm$ therefore depends on the sign of b:

- If $b > 0$, then $E_\pm$ exists only for $a < 0$, in which case $\lambda = \pm i\sqrt{-2a}$ and they are centers.
- If $b < 0$, then $E_\pm$ exists only for $a > 0$, in which case $\lambda = \pm\sqrt{2a} \in \mathbb{R}$ and they are saddles.

Both signs of b are covered by the classification above. The continuations and phase portraits of Figures 1–3 are drawn for $b > 0$, where the origin exchanges stability with a symmetric pair of centers; for $b < 0$, the effective potential $V(z) = \frac{1}{2}az^2 + \frac{1}{4}bz^4$ is unbounded below and $E_\pm$ are saddles when $a > 0$. The amplitude coefficient of the exact profiles constructed in Section 6 satisfies $\mu_1^2 = -2/b$, so that the reality of a profile $\Phi = \mu_1 U$ constrains the product of μ_1 with the amplitude factor of the corresponding Sardar function rather than μ_1 alone: The product is real either for $b < 0$ with a real factor, or for $b > 0$ with an imaginary factor, as happens for the sech_{pq} profile of Case I (in Section 6) with $pq > 0$; the reality and boundedness of each complete profile require, in addition, that the corresponding generalized function be free of real poles. Both sign regimes of b therefore carry exact solutions and are treated in Subsection 5.3: The portraits of the present section ($b > 0$) display the regime of the Case I soliton (presented in Section 6), while the regime $b < 0$ with $a = -r_1$ carries the Case III kink (presented in Section 6).

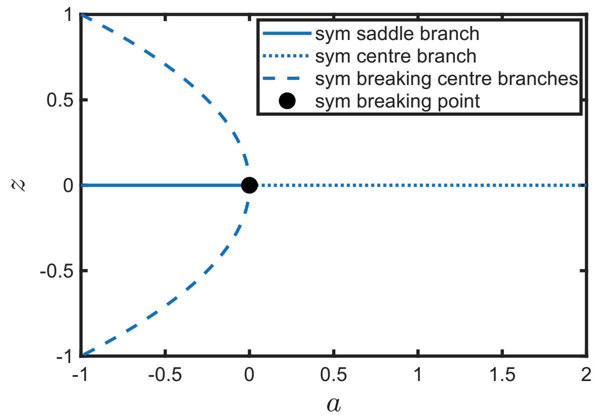

Figure 1. One-parameter continuation of equilibria in the (a, z)-plane for $b = 1$. The trivial symmetric branch $z = 0$ changes from a center branch for $a > 0$ to a saddle branch for $a < 0$. Two symmetry-breaking center branches bifurcate from $(0, 0)$, forming a Hamiltonian pitchfork. The crossing $a = 0$ marks the threshold at which the reduced amplitude equation passes from a single symmetric equilibrium to a symmetry-broken pair.

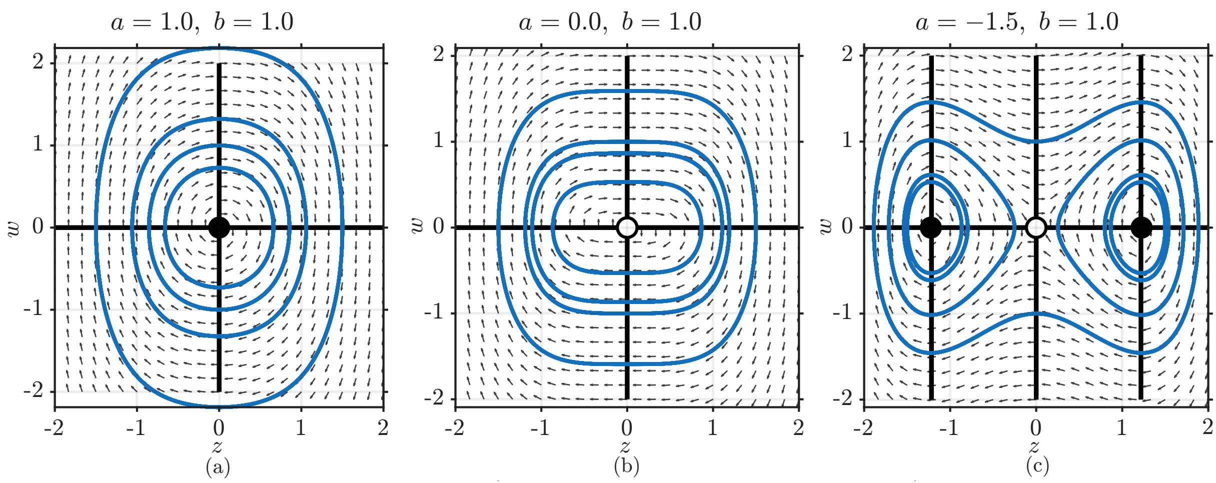

Figure 2. Phase portraits of the reduced system for $b = 1$ and representative values of a: (a) $a > 0$, showing a single center with nested periodic orbits; (b) $a = 0$, illustrating the degenerate transition; (c) $a < 0$, where the origin becomes a saddle and two symmetric centers emerge, separated by a figure-eight separatrix formed by a pair of homoclinic orbits to the origin. These portraits are computed for $b > 0$, the regime carrying the Case I sech_{pq} soliton (presented in Section 6), which is precisely the homoclinic loop of panel (c); the complementary regime $b < 0$, carrying the Case III $\tanh_{pq}$ kink (presented in Section 6), is treated in Subsection 5.3.

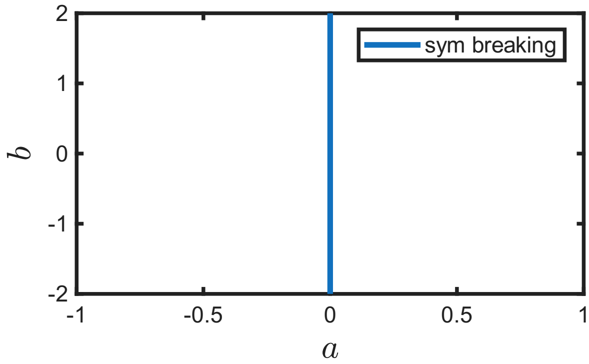

Figure 3. Symmetry-breaking set of Eq (5.1) in the two-parameter plane (a, b), computed by the symmetry-extended continuation of Subsection 5.4. The numerical branch coincides with the line $a = 0$ to machine precision, in agreement with the analytical prediction (5.10).

5.2. The Hamiltonian pitchfork at $a = 0$

For $b > 0$, the local analysis of Subsection 5.1 already determines the bifurcation. As a decreases through the critical value $a_c = 0$, the equilibrium E_0 exchanges stability from a center to a saddle, and a symmetric pair of centers $E_\pm$ is emitted along the antisymmetric isotype of the $\mathbb{Z}_2$-action. This is a Hamiltonian pitchfork bifurcation: A generic dissipative pitchfork is not available in this setting because volume preservation forbids attracting equilibria, and the bifurcating branches inherit the neutral stability characteristic of Hamiltonian centers [18]. The transition is degenerate at the linear level. At $a = 0$ the Jacobian matrix (5.5) at E_0 becomes

$$J(0,0)\Big|_{a=0} = \begin{pmatrix} 0 & 1 \\ 0 & 0 \end{pmatrix},$$

which is nilpotent with a defective double zero eigenvalue. The kernel of $J(0,0)$ itself is one-dimensional, spanned by the antisymmetric mode $(1,0)^{\mathsf{T}}$; the second vector of the Jordan chain is a generalized eigenvector, not a second zero mode. The two-dimensional null space relevant for branch-point continuation is that of the extended Jacobian $\left[\, J(0,0) \;\middle|\; \partial_a f \,\right]$ on the trivial branch, whose null directions are the tangent to the trivial branch, lying in the symmetric component (the parameter a is invariant under the $\mathbb{Z}_2$-action), and the antisymmetric symmetry-breaking direction; the two lie in distinct isotypic components, and only the antisymmetric direction drives the symmetry-breaking branch [22]. This isotypic splitting of the extended kernel is benign for the local analysis just performed, but it is exactly the feature that obstructs a naive numerical continuation of the symmetry-breaking locus in two-parameter space, as we discuss in Subsection 5.4. The global reorganization of the trajectories accompanying this transition is shown in Figure 2, again for $b > 0$, the single center of panel (a) is replaced, for $a < 0$, by a saddle at the origin together with two symmetric centers, separated by a figure-eight separatrix.

5.3. Classification in the parameter regime of the exact solutions

We now specialize the classification of Subsection 5.1 to the parameter regime carried by the exact profiles of Section 6. The balance of the Sardar-subequation ansatz gives

$$a = -r_1, \qquad \mu_1^2 = -\frac{2}{b}. \tag{5.6}$$

The reality of a profile $\Phi = \mu_1 U$ constrains the product of μ_1 with the amplitude factor of U rather than μ_1 alone, and two branches arise: Either $b < 0$, equivalently $\tau_1\tau_2 < 0$ (with the branch $\tau_1 < 0$ selected in the construction of the solutions, this gives $\tau_2 > 0$), on which μ_1 is real and the Sardar factor must itself be real; or $b > 0$ ($\tau_2 < 0$), on which μ_1 is imaginary and a real profile requires the Sardar factor to be imaginary as well. The second branch is realized by the sech_{pq} profile of Case I (presented in Section 6) with $pq > 0$, and we treat it first.

The branch $b > 0$: the bright soliton of Case I. For $b > 0$ and $r_1 > 0$, hence $a = -r_1 < 0$, the phase plane is exactly that of Figure 2(c): The origin is a saddle, $E_\pm$ are centers, and the level set $H = 0$ is the figure-eight separatrix formed by the two homoclinic loops of the origin. With $pq > 0$ the factor $\sqrt{-pqr_1}$ is imaginary, the composite amplitude $\mu_1\sqrt{-pqr_1} = \pm\sqrt{2pqr_1/b}$ is real, and, since $pe^{\eta} + qe^{-\eta} = 2\sqrt{pq}\cosh(\eta + \frac{1}{2}\ln(p/q))$ for $p, q > 0$, the profile reduces to

$$\Phi(\tau) = \pm\sqrt{\frac{2r_1}{b}}\ \operatorname{sech}\Big(\sqrt{r_1}\,\tau + \tfrac{1}{2}\ln(p/q)\Big), \tag{5.7}$$

a real, pole-free, exponentially localized pulse; the closed form (6.5) is correspondingly real, since $-2p_3\tau_2 pqr_1 > 0$ for $\tau_2 < 0$ and $p_3 > 0$. Its maximum amplitude $\sqrt{2r_1/b} = \sqrt{-2a/b}$ coincides with the intersection of the homoclinic loop with the z-axis obtained from $H = 0$, confirming that this profile *is* the homoclinic orbit: the bright optical soliton of the reduced system. (The csch_{pq} branch with $pq < 0$ reproduces the same profile, since $\operatorname{csch}_{p,q} = \operatorname{sech}_{p,-q}$; for $pq > 0$, its factor $\sqrt{pqr_1}$ is real and the corresponding profile is not real on this branch.) The remaining families carry real amplitude factors: $\sqrt{r_1/2}$ in Case IV and $\sqrt{-r_1/2}$ in Case III (presented in Section 6), and therefore yield purely imaginary profiles for $b > 0$; the Case II factor $\sqrt{-pqr_1}$ is imaginary for $pq < 0$ (see Section 6), but the generalized trigonometric functions are then complex-valued for generic real p, q, and their degenerate real sub-cases retain real poles, so no bounded profile arises there either. All of these families are excluded from this branch. The rest of this subsection treats the branch $b < 0$, on which μ_1 is real.

For $b < 0$, the effective potential $V(z) = \frac{1}{2}az^2 + \frac{1}{4}bz^4$ is unbounded below, so the corresponding phase portraits are dominated by escaping orbits and convey little beyond the equilibrium structure itself; we therefore describe this regime in words rather than reproducing further figures. Writing $b = -B$ with $B > 0$, the structure of the level sets is governed entirely by the sign of $a = -r_1$, and the four Sardar cases are classified as follows:

Cases I and IV ($r_1 > 0$, hence $a < 0$). Here, $-a/b < 0$, so the pair $E_\pm$ does not exist and the origin is the only equilibrium; by Subsection 5.1, it is a saddle. Since $V(z) \to -\infty$ as $|z| \to \infty$, the nontrivial branches of the level set $H = 0$ are unbounded and no homoclinic loop is present. The sech_{pq} and csch_{pq} profiles of Case I (presented in Section 6) therefore lie on the unbounded branches of the invariant manifolds of the saddle and must not be interpreted as homoclinic solutions in this regime. The homoclinic realization of the sech_{pq} profile belongs to the branch $b > 0$ treated above. The $\tan_{pq}$ and $\cot_{pq}$ profiles of Case IV (presented in Section 6) lie on the level $H = -r_1^2/(4b) > 0$, which is likewise unbounded; they are periodic but possess regularly repeated real poles, so their periodicity does not imply boundedness.

Cases II and III ($r_1 < 0$, hence $a > 0$). Here, $-a/b > 0$, so $E_\pm = (\pm\sqrt{a/B}, 0)$ exists and, by Subsection 5.1, are saddles, while the origin is a center. The level set through the saddles is

$$H(E_\pm) = -\frac{a^2}{4b} = \frac{a^2}{4B}, \tag{5.8}$$

in agreement with the general relation $H = -r_0/b$, since for Case III one has $r_0 = r_1^2/4$ and $a^2 = r_1^2$ (see Section 6). The $\tanh_{pq}$ profile of Case III (presented in Section 6) lies on this level set and satisfies $\Phi(\tau) \to \pm\sqrt{a/B}$ as $\tau \to \pm\infty$, these being precisely the coordinates of $E_\pm$; it is therefore the heteroclinic connection joining the two saddles, and, under the condition that its denominator has no real zero, it is a regular bounded kink-type traveling wave. The associated $\coth_{pq}$ branch lies on the same level set but on its exterior branch and is singular. The $\sec_{pq}$ and $\csc_{pq}$ profiles of Case II (presented in Section 6) lie instead on the level $H = -r_0/b = 0$, which for $a > 0$ and $b < 0$ consists of the center E_0 together with two unbounded branches beginning at $z = \pm\sqrt{2a/B}$; these profiles are likewise singular.

The classification above shows that the Hamiltonian level alone does not determine the admissibility of a profile. The equilibrium structure of the reduced system, the topology of the corresponding level set, and the domain and singularity structure of the explicit generalized function must be considered together. Applying these three criteria to the profiles of Section 6 leaves two regular bounded traveling waves: The sech_{pq} soliton of Case I on the branch $b > 0$, $pq > 0$, and the $\tanh_{pq}$ kink of Case III on the branch $b < 0$, $pq > 0$; all remaining profiles are exact but singular, and are formal traveling-wave solutions of the reduced equation.

5.4. Continuation of the symmetry-breaking

The symmetry-breaking locus of Eq (5.1) is the line $a = 0$, and this is immediate from Subsection 5.1; nothing in the analysis of the Fokas system requires a numerical computation of it. The purpose of this subsection is therefore not to obtain the locus, but to verify an equivariant continuation scheme on a problem whose answer is known in closed form. The defining system at an equivariant branch point is degenerate, and it is useful to see that degeneracy resolved against a ground truth before the same scheme is applied where no closed form is available. A reader interested only in the Fokas system may proceed directly to Section 6.

Obstruction to standard branch-point continuation. At the bifurcation point, the linearization of Eq (5.1) about E_0 has the defective double zero eigenvalue identified in Subsection 5.2, with kernel split by the $\mathbb{Z}_2$-action into a symmetric and an antisymmetric component. Generic branch-point continuation, going back to Werner and Spence [23] and standardized in the bordered-system treatment of Govaerts [24], is formulated under the assumption that the kernel of the bordered defining system is one-dimensional; this assumption underlies the implementations in the numerical continuation packages MatCont (Matlab continuation toolbox) [25], coco (computational continuation core) [26] and DDE-Biftool (bifurcation tool for delay differential equations, DDEs) [27,28]. In the equivariant setting it fails, and a direct continuation of the symmetry-breaking set from the symmetric branch is consequently not well posed without explicit account of the isotypic decomposition.

Symmetry-extended defining system. The remedy, due in the periodic-orbit context to Wulff and Schebesch [20] and adapted to G-equivariant delay equations in [19], is to encode the symmetry decomposition into the defining system itself: The continued solution is constrained to lie in $\mathrm{Fix}(\mathbb{Z}_2)$, while the critical eigenvector is left free to point in the symmetry-breaking direction transverse to it. Concretely, this is achieved by appending the linear constraint

$$P_{\mathrm{sy}}(\rho(\gamma)\,x - x) \;=\; 0, \tag{5.9}$$

to the equilibrium equation, where P_{sy} is the projection onto the symmetric isotype and $\rho(\gamma) = -I_2$ is the representation of $\mathcal{R}$; for the present problem, (5.9) reduces to $x = 0$. The eigenvector equation is left unconstrained, so that the critical mode is permitted to lie in the antisymmetric isotype–the distinction that makes the formulation work, and the same one that underlies the equivariant defining systems analyzed in [19, 20]. We adopt this formulation in the ODE limit by setting the delay to zero in the DDE-BIFTOOL-based implementation of [19, 28]. With this formulation, the symmetry-breaking set continues cleanly in the (a, b) plane. The computed locus is

$$\{(a, b) : a = 0\}, \tag{5.10}$$

recovered to machine precision in a; after removal of plotting noise from roundoff, the numerical branch is the vertical line $a = 0$, in exact agreement with the analytical prediction. The result is shown in Figure 3. The value of the exercise lies in this agreement: The underlying continuation problem retains the characteristic degeneracy of an equivariant branch point [23, 24], namely, a symmetric branch on which the bordered Jacobian has a two-dimensional kernel split by the group action, and the symmetry-extended formulation of [19, 20] resolves it on a model whose answer is known in advance.

Remark 5.1. *The phase-plane geometry depends essentially on the sign of b. In particular, the double-well configuration with a figure-eight homoclinic separatrix occurs for $b > 0$ and $a < 0$. This is the parameter regime used in Figures 1–3, and it is not merely illustrative: It carries the Case I* sech_{pq} *soliton, which is precisely the homoclinic loop of the figure-eight (Subsection 5.3). The real-μ_1 branch of the exact Sardar-subequation solutions requires instead $b < 0$ and carries the Case III kink (presented in Section 6); the homoclinic figure-eight structure must not be transferred to that branch. For $b < 0$, the effective potential*

$$V(z) = \frac{1}{2}az^2 + \frac{1}{4}bz^4 \tag{5.11}$$

is unbounded below, and the equilibrium and Hamiltonian-level classification must be reconsidered according to the sign of $a = -r_1$.

6. Exact solutions

First, we find the value of ρ presented in Eq (3.5) by balancing between Φ'' and Φ^3 in Eq (4.7). This leads to $\rho = 1$. Hence, Eq (3.5) becomes

$$\Phi(\tau) = \sum_{i=0}^{1} \mu_i U^i(\tau) = \mu_0 + \mu_1 U(\tau). \tag{6.1}$$

Substituting Eq (6.1) along with Eq (3.6) into Eq (4.7) ends up with an algebraic equation, taking the coefficients of U^j, $\forall j$ to have a system of equations whose solutions are

$$\mu_0 = 0, \quad \mu_1 = \pm\frac{\sqrt{2p_3\tau_2}\, p_1^{\frac{1}{4}}(p_1w_1^2 + w_3)^{\frac{1}{4}}}{\sqrt{p_2p_4}\, r_1^{\frac{1}{4}}}, \quad \tau_1 = -\frac{\sqrt{p_1w_1^2 + w_3}}{\sqrt{p_1r_1}}. \tag{6.2}$$

For Cases II and III below, where $r_1 < 0$, the expression for τ_1 in Eq (6.2) is real only if $p_1w_1^2 + w_3 < 0$ (taking $p_1 > 0$); the ratio $(p_1w_1^2 + w_3)/r_1$ is then positive, and the factors $(p_1w_1^2 + w_3)^{1/4}/r_1^{1/4}$ appearing in μ_1 and in the amplitudes listed below are to be read as $((p_1w_1^2 + w_3)/r_1)^{1/4}$, which is real. Using

$U'' = r_1 U + 2U^3$ (obtained by differentiating Eq (3.6)), the coefficients of U and U^3 in Eq (4.7) vanish precisely when

$$a = -r_1, \qquad \mu_1^2 = -\frac{2}{b}. \tag{6.3}$$

The relation $a = -r_1$ is exactly the choice of τ_1 recorded in Eq (6.2), while $\mu_1^2 = -2/b$ fixes the amplitude. Each closed-form profile listed below was verified by direct back-substitution into Eq (4.7) (the residual vanishes identically), and the corresponding fields $H = \Phi e^{iw}$, $G = (p_4\tau_1/p_3\tau_2)\Phi^2$ were checked to satisfy the original system (1.1) once the compatibility relations $\tau_3 = -2p_1 w_1 \tau_1$ from Eqs (4.3) and (4.6) are imposed.

Equation (6.3) determines the admissible parameter regime, and we record it before listing the profiles. Since Φ is the physical amplitude, the product of μ_1 with the amplitude factor of the chosen Sardar function must be real; this occurs either with both factors real or with both factors imaginary. On the first branch, μ_1 is real, and $\mu_1^2 = -2/b > 0$ requires

$$b < 0, \qquad \text{equivalently, by (4.8),} \qquad \tau_1\tau_2 < 0. \tag{6.4}$$

With the branch $\tau_1 < 0$ fixed by Eq (6.2), this means $\tau_2 > 0$; the expression for μ_1 in (6.2) is then real, as it must be. On the second branch, $b > 0$ ($\tau_2 < 0$), the coefficient μ_1 is imaginary, and $\Phi = \mu_1 U$ is real precisely when the amplitude factor of U is imaginary as well. Among the families of Section 3 this occurs only for the sech_{pq} branch of Case I with $pq > 0$ (equivalently for the csch_{pq} branch with $pq < 0$, since $\mathrm{csch}_{p,q} = \mathrm{sech}_{p,-q}$): The closed form (6.5) is then manifestly real, because $-2p_3\tau_2 pqr_1 > 0$ for $\tau_2 < 0$, $pq > 0$, and $p_3 > 0$; the function sech_{pq} is pole-free for $p, q > 0$; and the resulting profile is the bright soliton of Subsection 5.3, Eq (5.7). No further bounded profiles arise on this branch: The amplitude factors of Cases III and IV are real, so their profiles are purely imaginary for $b > 0$, while the Case II factor is imaginary only for $pq < 0$, where the generalized trigonometric functions are complex-valued for generic real p, q and reduce, in the degenerate real sub-cases, to singular profiles with real poles. Together with $a = -r_1$, the sign of r_1 determines the relevant Sardar-subequation family. Nevertheless, the sign conditions on b and r_1 are not sufficient by themselves to establish boundedness. The complete profile must also satisfy the reality and domain conditions of the corresponding generalized function. In particular, a real amplitude coefficient does not preclude poles in the generalized hyperbolic or trigonometric factors. We therefore classify each profile separately according to its reality, domain of definition, and boundedness. Profiles whose generalized functions possess real poles are exact solutions of the reduced equation but are not bounded, and we refer to them below as formal traveling-wave solutions, reserving the terms solitary wave, soliton, and optical pulse for the bounded profiles. The classification is summarized in Table 1.

The remainder of this discussion concerns the real-μ_1 branch $b < 0$; the complementary branch $b > 0$, $pq > 0$, carrying the bounded sech_{pq} soliton, was recorded above. The condition

$$\mu_1^2 = -\frac{2}{b} > 0$$

ensures that the amplitude coefficient μ_1 is real and, consequently, requires $b < 0$. However, this condition guarantees only the reality of the constant amplitude coefficient and does not, by itself, ensure that the complete traveling-wave profile is real, globally defined, or bounded. Therefore, the reality and boundedness of each obtained solution must be examined separately by considering the corresponding generalized Sardar function and its denominator.

Table 1. Domain, pole structure, and dynamical classification of the Sardar-subequation traveling-wave profiles. Except for the second row, all entries refer to the real-μ_1 branch $b < 0$ of Eq (6.4); the second row records the branch $b > 0$, on which μ_1 and the Case I amplitude factor are simultaneously imaginary and the composite amplitude is real for $pq > 0$.

Case	**Condition**	**Profile**	**Domain/Poles**	**Classification**
I	$r_1 > 0,\ r_0 = 0$	sech_{pq}	Real pole for $pq < 0$	Singular formal solution
I	$r_1 > 0,\ r_0 = 0,\ b > 0,\ pq > 0$	sech_{pq}	No real poles ($p, q > 0$)	Regular bounded soliton
I	$r_1 > 0,\ r_0 = 0$	csch_{pq}	Real poles when $q/p > 0$	Singular formal solution
II	$r_1 < 0,\ r_0 = 0$	$\sec_{pq}$	Periodic real poles	Singular periodic solution
II	$r_1 < 0,\ r_0 = 0$	$\csc_{pq}$	Periodic real poles	Singular periodic solution
III	$r_1 < 0,\ r_0 = r_1^2/4$	$\tanh_{pq}$	No real poles if $pq > 0$	Regular bounded kink
III	$r_1 < 0,\ r_0 = r_1^2/4$	$\coth_{pq}$	Real poles when $q/p > 0$	Singular formal solution
IV	$r_1 > 0,\ r_0 = r_1^2/4$	$\tan_{pq}$	Periodic real poles	Singular periodic solution
IV	$r_1 > 0,\ r_0 = r_1^2/4$	$\cot_{pq}$	Periodic real poles	Singular periodic solution

For real parameters p and q, the generalized hyperbolic functions considered in this work are defined by

$$\mathrm{sech}_{pq}(\eta) = \frac{2}{pe^{\eta} + qe^{-\eta}}, \qquad \mathrm{csch}_{pq}(\eta) = \frac{2}{pe^{\eta} - qe^{-\eta}},$$

and

$$\tanh_{pq}(\eta) = \frac{pe^{\eta} - qe^{-\eta}}{pe^{\eta} + qe^{-\eta}}, \qquad \coth_{pq}(\eta) = \frac{pe^{\eta} + qe^{-\eta}}{pe^{\eta} - qe^{-\eta}}.$$

Accordingly, a traveling-wave profile is regarded as a real regular solution only when all of its amplitude factors are real and the denominator of the corresponding generalized function does not vanish on the considered real traveling coordinate. Moreover, the profile is called bounded if

$$\sup_{\eta \in \mathbb{R}} |\Phi(\eta)| < \infty.$$

If the denominator of the generalized function vanishes at any real value of η, the corresponding solution possesses a pole and is therefore classified as a singular formal solution on the intervals separated by its poles.

For Case I, where $r_1 > 0$, the sech_{pq} solution contains the amplitude factor $\sqrt{-pqr_1}$. For real p and q, the reality of this factor requires $pq < 0$. However, under this condition, the denominator of $\mathrm{sech}_{pq}(\eta)$,

$$pe^{\eta} + qe^{-\eta},$$

vanishes at

$$\eta_* = \frac{1}{2} \ln\left(-\frac{q}{p}\right),$$

provided that $-q/p > 0$. Hence, the corresponding sech_{pq} profile possesses a real pole. Consequently, for real p and q, the Case I sech_{pq} branch cannot be regarded as a globally bounded real solitary-wave solution under the parameter conditions required for a real amplitude coefficient μ_1; its bounded solitary-wave realization belongs instead to the branch $b > 0$, $pq > 0$ recorded above.

Similarly, the csch_{pq} branch has a pole whenever

$$pe^{\eta} - qe^{-\eta} = 0,$$

which occurs at

$$\eta_* = \frac{1}{2}\ln\left(\frac{q}{p}\right),$$

provided that $q/p > 0$. Thus, the corresponding csch_{pq} solution is classified as a singular formal traveling-wave solution.

For Case III, the $\tanh_{pq}$ branch is given by

$$\tanh_{pq}(\eta) = \frac{pe^{\eta} - qe^{-\eta}}{pe^{\eta} + qe^{-\eta}}.$$

If $pq > 0$, then

$$pe^{\eta} + qe^{-\eta} \neq 0, \qquad \eta \in \mathbb{R},$$

and hence the $\tanh_{pq}$ profile has no real poles. Furthermore,

$$\lim_{\eta \to +\infty} \tanh_{pq}(\eta) = \operatorname{sgn}(p),$$

and

$$\lim_{\eta \to -\infty} \tanh_{pq}(\eta) = -\operatorname{sgn}(q).$$

Therefore, under the above parameter restriction, the $\tanh_{pq}$ profile is real and bounded and represents a regular kink-type traveling wave, provided that the remaining amplitude and model parameters satisfy the required reality conditions.

In contrast, the $\coth_{pq}$ branch possesses poles whenever

$$pe^{\eta} - qe^{-\eta} = 0.$$

Therefore, this branch is classified as a singular formal solution. The generalized trigonometric profiles are treated in the same manner: Although they are periodic, their denominators may vanish at a discrete sequence of real values of the traveling coordinate. Thus, periodicity alone does not imply boundedness, and such profiles are classified as singular periodic traveling-wave solutions whenever real poles are present.

Consequently, the condition $b < 0$ should be interpreted only as the condition ensuring the reality of the amplitude coefficient μ_1. The complete admissibility of a traveling-wave profile requires, in addition, the verification of its real-valuedness, domain of definition, absence of real poles, and boundedness. This distinction allows us to separate regular bounded traveling waves from formal singular solutions and provides a mathematically precise classification of the obtained solution families.

Now, the traveling wave solutions are given as follows.

Case I: If $r_1 > 0$ and $r_0 = 0$, then

$$\Phi_1^{\pm}(\tau) = \pm \frac{\sqrt{-2p_3\tau_2 pqr_1}\, p_1^{\frac{1}{4}}(p_1 w_1^2 + w_3)^{\frac{1}{4}}}{\sqrt{p_2 p_4}\, r_1^{\frac{1}{4}}} \operatorname{sech}_{pq}(\sqrt{r_1}\,\tau),$$

$$\Phi_2^{\pm}(\tau) = \pm \frac{\sqrt{2p_3\tau_2 pqr_1}\, p_1^{\frac{1}{4}}(p_1w_1^2 + w_3)^{\frac{1}{4}}}{\sqrt{p_2p_4}\, r_1^{\frac{1}{4}}} \operatorname{csch}_{pq}(\sqrt{r_1}\,\tau).$$

Hence, the traveling wave solutions can be written as follows:

$$H_1^{\pm}(x,y,t) = \pm \frac{\sqrt{-2p_3\tau_2 pqr_1}\, p_1^{\frac{1}{4}}(p_1w_1^2 + w_3)^{\frac{1}{4}}}{\sqrt{p_2p_4}\, r_1^{\frac{1}{4}}} \operatorname{sech}_{pq}\left(\sqrt{r_1}\left(\tau_1 x + \tau_2 y + \frac{\tau_3\Gamma(\beta+1)}{\delta}t^{\delta}\right)\right) \times e^{i\left(w_1x + w_2y + \frac{w_3\Gamma(\beta+1)}{\delta}t^{\delta}\right)}, \tag{6.5}$$

$$G_1^{\pm}(x,y,t) = \frac{p_4\tau_1}{p_3\tau_2}\Phi_1^2\left(\tau_1 x + \tau_2 y + \frac{\tau_3\Gamma(\beta+1)}{\delta}t^{\delta}\right),$$

$$H_2^{\pm}(x,y,t) = \pm \frac{\sqrt{2p_3\tau_2 pqr_1}\, p_1^{\frac{1}{4}}(p_1w_1^2 + w_3)^{\frac{1}{4}}}{\sqrt{p_2p_4}\, r_1^{\frac{1}{4}}} \operatorname{csch}_{pq}\left(\sqrt{r_1}\left(\tau_1 x + \tau_2 y + \frac{\tau_3\Gamma(\beta+1)}{\delta}t^{\delta}\right)\right) \times e^{i\left(w_1x + w_2y + \frac{w_3\Gamma(\beta+1)}{\delta}t^{\delta}\right)}, \tag{6.6}$$

$$G_2^{\pm}(x,y,t) = \frac{p_4\tau_1}{p_3\tau_2}\left(\pm \frac{\sqrt{2p_3\tau_2 pqr_1}\, p_1^{\frac{1}{4}}(p_1w_1^2 + w_3)^{\frac{1}{4}}}{\sqrt{p_2p_4}\, r_1^{\frac{1}{4}}} \operatorname{csch}_{pq}\left(\sqrt{r_1}\left(\tau_1 x + \tau_2 y + \frac{\tau_3\Gamma(\beta+1)}{\delta}t^{\delta}\right)\right)\right)^2. \tag{6.7}$$

Case II: If $r_1 < 0$ and $r_0 = 0$, then

$$\Phi_3^{\pm}(\tau) = \pm \frac{\sqrt{-2p_3\tau_2 pqr_1}\, p_1^{\frac{1}{4}}(p_1w_1^2 + w_3)^{\frac{1}{4}}}{\sqrt{p_2p_4}\, r_1^{\frac{1}{4}}} \sec_{pq}(\sqrt{-r_1}\,\tau),$$

$$\Phi_4^{\pm}(\tau) = \pm \frac{\sqrt{-2p_3\tau_2 pqr_1}\, p_1^{\frac{1}{4}}(p_1w_1^2 + w_3)^{\frac{1}{4}}}{\sqrt{p_2p_4}\, r_1^{\frac{1}{4}}} \csc_{pq}(\sqrt{-r_1}\,\tau).$$

Therefore, the traveling wave solutions can be written as follows:

$$H_3^{\pm}(x,y,t) = \pm \frac{\sqrt{-2p_3\tau_2 pqr_1}\, p_1^{\frac{1}{4}}(p_1w_1^2 + w_3)^{\frac{1}{4}}}{\sqrt{p_2p_4}\, r_1^{\frac{1}{4}}} \sec_{pq}\left(\sqrt{-r_1}\left(\tau_1 x + \tau_2 y + \frac{\tau_3\Gamma(\beta+1)}{\delta}t^{\delta}\right)\right) \times e^{i\left(w_1x + w_2y + \frac{w_3\Gamma(\beta+1)}{\delta}t^{\delta}\right)},$$

$$H_4^{\pm}(x,y,t) = \pm \frac{\sqrt{-2p_3\tau_2 pqr_1}\, p_1^{\frac{1}{4}}(p_1w_1^2 + w_3)^{\frac{1}{4}}}{\sqrt{p_2p_4}\, r_1^{\frac{1}{4}}} \csc_{pq}\left(\sqrt{-r_1}\left(\tau_1 x + \tau_2 y + \frac{\tau_3\Gamma(\beta+1)}{\delta}t^{\delta}\right)\right) \times e^{i\left(w_1x + w_2y + \frac{w_3\Gamma(\beta+1)}{\delta}t^{\delta}\right)},$$

$$G_j^{\pm}(x,y,t) = \frac{p_4\tau_1}{p_3\tau_2}\Phi_j^2\left(\tau_1 x + \tau_2 y + \frac{\tau_3\Gamma(\beta+1)}{\delta}t^{\delta}\right), \qquad \forall j = 3, 4.$$

Case III: If $r_1 < 0$ and $r_0 = \frac{r_1^2}{4}$, then

$$\Phi_5^{\pm}(\tau) = \pm\frac{\sqrt{-p_3\tau_2 r_1}\,p_1^{\frac{1}{4}}(p_1w_1^2+w_3)^{\frac{1}{4}}}{\sqrt{p_2p_4}\,r_1^{\frac{1}{4}}}\ \tanh_{pq}\!\left(\sqrt{-\frac{r_1}{2}}\tau\right),$$

$$\Phi_6^{\pm}(\tau) = \pm\frac{\sqrt{-p_3\tau_2 r_1}\,p_1^{\frac{1}{4}}(p_1w_1^2+w_3)^{\frac{1}{4}}}{\sqrt{p_2p_4}\,r_1^{\frac{1}{4}}}\ \coth_{pq}\!\left(\sqrt{-\frac{r_1}{2}}\tau\right),$$

$$\Phi_7^{\pm}(\tau) = \pm\frac{\sqrt{-p_3\tau_2 r_1}\,p_1^{\frac{1}{4}}(p_1w_1^2+w_3)^{\frac{1}{4}}}{\sqrt{p_2p_4}\,r_1^{\frac{1}{4}}}\ \left(\tanh_{pq}\!\left(\sqrt{-2r_1}\tau\right) \pm i\sqrt{pq}\,sech_{pq}\!\left(\sqrt{-2r_1}\tau\right)\right),$$

$$\Phi_8^{\pm}(\tau) = \pm\frac{\sqrt{-p_3\tau_2 r_1}\,p_1^{\frac{1}{4}}(p_1w_1^2+w_3)^{\frac{1}{4}}}{\sqrt{p_2p_4}\,r_1^{\frac{1}{4}}}\ \left(\coth_{pq}\!\left(\sqrt{-2r_1}\tau\right) \pm \sqrt{pq}\,csch_{pq}\!\left(\sqrt{-2r_1}\tau\right)\right),$$

$$\Phi_9^{\pm}(\tau) = \pm\frac{\sqrt{-p_3\tau_2 r_1}\,p_1^{\frac{1}{4}}(p_1w_1^2+w_3)^{\frac{1}{4}}}{2\sqrt{p_2p_4}\,r_1^{\frac{1}{4}}}\ \left(\tanh_{pq}\!\left(\sqrt{-\frac{r_1}{8}}\tau\right) + coth_{pq}\!\left(\sqrt{-\frac{r_1}{8}}\tau\right)\right).$$

Thus, the traveling wave solutions are

$$\begin{aligned}H_5^{\pm}(x,y,t) = &\pm\frac{\sqrt{-p_3\tau_2 r_1}\,p_1^{\frac{1}{4}}(p_1w_1^2+w_3)^{\frac{1}{4}}}{\sqrt{p_2p_4}\,r_1^{\frac{1}{4}}}\ \tanh_{pq}\!\left(\sqrt{-\frac{r_1}{2}}\left(\tau_1x+\tau_2y+\frac{\tau_3\Gamma(\beta+1)}{\delta}t^{\delta}\right)\right)\\ &\times e^{i\left(w_1x+w_2y+\frac{w_3\Gamma(\beta+1)}{\delta}t^{\delta}\right)},\end{aligned}$$

$$\begin{aligned}H_6^{\pm}(x,y,t) = &\pm\frac{\sqrt{-p_3\tau_2 r_1}\,p_1^{\frac{1}{4}}(p_1w_1^2+w_3)^{\frac{1}{4}}}{\sqrt{p_2p_4}\,r_1^{\frac{1}{4}}}\ \coth_{pq}\!\left(\sqrt{-\frac{r_1}{2}}\left(\tau_1x+\tau_2y+\frac{\tau_3\Gamma(\beta+1)}{\delta}t^{\delta}\right)\right)\\ &\times e^{i\left(w_1x+w_2y+\frac{w_3\Gamma(\beta+1)}{\delta}t^{\delta}\right)},\end{aligned}$$

$$\begin{aligned}H_7^{\pm}(x,y,t) = &\pm\frac{\sqrt{-p_3\tau_2 r_1}\,p_1^{\frac{1}{4}}(p_1w_1^2+w_3)^{\frac{1}{4}}}{\sqrt{p_2p_4}\,r_1^{\frac{1}{4}}}\ \left(\tanh_{pq}\!\left(\sqrt{-2r_1}\left(\tau_1x+\tau_2y+\frac{\tau_3\Gamma(\beta+1)}{\delta}t^{\delta}\right)\right)\right.\\ &\left.\pm i\sqrt{pq}\,sech_{pq}\!\left(\sqrt{-2r_1}\left(\tau_1x+\tau_2y+\frac{\tau_3\Gamma(\beta+1)}{\delta}t^{\delta}\right)\right)\right)e^{i\left(w_1x+w_2y+\frac{w_3\Gamma(\beta+1)}{\delta}t^{\delta}\right)},\end{aligned}$$

$$\begin{aligned}H_8^{\pm}(x,y,t) = &\pm\frac{\sqrt{-p_3\tau_2 r_1}\,p_1^{\frac{1}{4}}(p_1w_1^2+w_3)^{\frac{1}{4}}}{\sqrt{p_2p_4}\,r_1^{\frac{1}{4}}}\ \left(\coth_{pq}\!\left(\sqrt{-2r_1}\left(\tau_1x+\tau_2y+\frac{\tau_3\Gamma(\beta+1)}{\delta}t^{\delta}\right)\right)\right.\\ &\left.\pm\sqrt{pq}\,csch_{pq}\!\left(\sqrt{-2r_1}\left(\tau_1x+\tau_2y+\frac{\tau_3\Gamma(\beta+1)}{\delta}t^{\delta}\right)\right)\right)e^{i\left(w_1x+w_2y+\frac{w_3\Gamma(\beta+1)}{\delta}t^{\delta}\right)},\end{aligned}$$

$$\begin{aligned}H_9^{\pm}(x,y,t) = &\pm\frac{\sqrt{-p_3\tau_2 r_1}\,p_1^{\frac{1}{4}}(p_1w_1^2+w_3)^{\frac{1}{4}}}{2\sqrt{p_2p_4}\,r_1^{\frac{1}{4}}}\ \left(\tanh_{pq}\!\left(\sqrt{-\frac{r_1}{8}}\left(\tau_1x+\tau_2y+\frac{\tau_3\Gamma(\beta+1)}{\delta}t^{\delta}\right)\right)\right.\\ &\left.+coth_{pq}\!\left(\sqrt{-\frac{r_1}{8}}\left(\tau_1x+\tau_2y+\frac{\tau_3\Gamma(\beta+1)}{\delta}t^{\delta}\right)\right)\right)e^{i\left(w_1x+w_2y+\frac{w_3\Gamma(\beta+1)}{\delta}t^{\delta}\right)},\end{aligned}$$

$$G_j^{\pm}(x,y,t)=\frac{p_4\tau_1}{p_3\tau_2}\Phi_j^2\left(\tau_1x+\tau_2y+\frac{\tau_3\Gamma(\beta+1)}{\delta}t^{\delta}\right),\qquad \forall j=5,6,7,8,9.$$

Case IV: If $r_1>0$ and $r_0=\frac{r_1^2}{4}$, then

$$\Phi_{10}^{\pm}(\tau)=\pm\frac{\sqrt{p_3\tau_2r_1}p_1^{\frac{1}{4}}(p_1w_1^2+w_3)^{\frac{1}{4}}}{\sqrt{p_2p_4}r_1^{\frac{1}{4}}}\ \tan_{pq}\left(\sqrt{\frac{r_1}{2}}\tau\right),$$

$$\Phi_{11}^{\pm}(\tau)=\pm\frac{\sqrt{p_3\tau_2r_1}p_1^{\frac{1}{4}}(p_1w_1^2+w_3)^{\frac{1}{4}}}{\sqrt{p_2p_4}r_1^{\frac{1}{4}}}\ \cot_{pq}\left(\sqrt{\frac{r_1}{2}}\tau\right),$$

$$\Phi_{12}^{\pm}(\tau)=\pm\frac{\sqrt{p_3\tau_2r_1}p_1^{\frac{1}{4}}(p_1w_1^2+w_3)^{\frac{1}{4}}}{\sqrt{p_2p_4}r_1^{\frac{1}{4}}}\ \left(\tan_{pq}\left(\sqrt{2r_1}\tau\right)\pm\sqrt{pq}\,sec_{pq}\left(\sqrt{2r_1}\tau\right)\right),$$

$$\Phi_{13}^{\pm}(\tau)=\pm\frac{\sqrt{p_3\tau_2r_1}p_1^{\frac{1}{4}}(p_1w_1^2+w_3)^{\frac{1}{4}}}{\sqrt{p_2p_4}r_1^{\frac{1}{4}}}\ \left(\cot_{pq}\left(\sqrt{2r_1}\tau\right)\pm\sqrt{pq}\,csc_{pq}\left(\sqrt{2r_1}\tau\right)\right),$$

$$\Phi_{14}^{\pm}(\tau)=\pm\frac{\sqrt{p_3\tau_2r_1}p_1^{\frac{1}{4}}(p_1w_1^2+w_3)^{\frac{1}{4}}}{2\sqrt{p_2p_4}r_1^{\frac{1}{4}}}\ \left(\tan_{pq}\left(\sqrt{\frac{r_1}{8}}\tau\right)+cot_{pq}\left(\sqrt{\frac{r_1}{8}}\tau\right)\right).$$

Hence, the traveling wave solutions are

$$H_{10}^{\pm}(x,y,t)=\pm\frac{\sqrt{p_3\tau_2r_1}p_1^{\frac{1}{4}}(p_1w_1^2+w_3)^{\frac{1}{4}}}{\sqrt{p_2p_4}r_1^{\frac{1}{4}}}\ \tan_{pq}\left(\sqrt{\frac{r_1}{2}}\left(\tau_1x+\tau_2y+\frac{\tau_3\Gamma(\beta+1)}{\delta}t^{\delta}\right)\right)\times e^{i\left(w_1x+w_2y+\frac{w_3\Gamma(\beta+1)}{\delta}t^{\delta}\right)},\tag{6.8}$$

$$H_{11}^{\pm}(x,y,t)=\pm\frac{\sqrt{p_3\tau_2r_1}p_1^{\frac{1}{4}}(p_1w_1^2+w_3)^{\frac{1}{4}}}{\sqrt{p_2p_4}r_1^{\frac{1}{4}}}\ \cot_{pq}\left(\sqrt{\frac{r_1}{2}}\left(\tau_1x+\tau_2y+\frac{\tau_3\Gamma(\beta+1)}{\delta}t^{\delta}\right)\right)\times e^{i\left(w_1x+w_2y+\frac{w_3\Gamma(\beta+1)}{\delta}t^{\delta}\right)},$$

$$H_{12}^{\pm}(x,y,t)=\pm\frac{\sqrt{p_3\tau_2r_1}p_1^{\frac{1}{4}}(p_1w_1^2+w_3)^{\frac{1}{4}}}{\sqrt{p_2p_4}r_1^{\frac{1}{4}}}\ \left(\tan_{pq}\left(\sqrt{2r_1}\left(\tau_1x+\tau_2y+\frac{\tau_3\Gamma(\beta+1)}{\delta}t^{\delta}\right)\right)\pm\sqrt{pq}\,sec_{pq}\left(\sqrt{2r_1}\left(\tau_1x+\tau_2y+\frac{\tau_3\Gamma(\beta+1)}{\delta}t^{\delta}\right)\right)\right)e^{i\left(w_1x+w_2y+\frac{w_3\Gamma(\beta+1)}{\delta}t^{\delta}\right)},$$

$$H_{13}^{\pm}(x,y,t)=\pm\frac{\sqrt{p_3\tau_2r_1}p_1^{\frac{1}{4}}(p_1w_1^2+w_3)^{\frac{1}{4}}}{\sqrt{p_2p_4}r_1^{\frac{1}{4}}}\ \left(\cot_{pq}\left(\sqrt{2r_1}\left(\tau_1x+\tau_2y+\frac{\tau_3\Gamma(\beta+1)}{\delta}t^{\delta}\right)\right)\pm\sqrt{pq}\,csc_{pq}\left(\sqrt{2r_1}\left(\tau_1x+\tau_2y+\frac{\tau_3\Gamma(\beta+1)}{\delta}t^{\delta}\right)\right)\right)e^{i\left(w_1x+w_2y+\frac{w_3\Gamma(\beta+1)}{\delta}t^{\delta}\right)},$$

$$H_{14}^{\pm}(x,y,t)=\pm\frac{\sqrt{p_3\tau_2r_1}p_1^{\frac{1}{4}}(p_1w_1^2+w_3)^{\frac{1}{4}}}{2\sqrt{p_2p_4}r_1^{\frac{1}{4}}}\ \left(\tan_{pq}\left(\sqrt{\frac{r_1}{8}}\left(\tau_1x+\tau_2y+\frac{\tau_3\Gamma(\beta+1)}{\delta}t^{\delta}\right)\right)\right.$$

$$+cot_{pq}\left(\sqrt{\frac{r_1}{8}}\left(\tau_1 x+\tau_2 y+\frac{\tau_3\Gamma(\beta+1)}{\delta}t^{\delta}\right)\right)\Bigg)e^{i\left(w_1 x+w_2 y+\frac{w_3\Gamma(\beta+1)}{\delta}t^{\delta}\right)},$$

$$G_j^{\pm}(x,y,t)=\frac{p_4\tau_1}{p_3\tau_2}\Phi_j^2\left(\tau_1 x+\tau_2 y+\frac{\tau_3\Gamma(\beta+1)}{\delta}t^{\delta}\right),\qquad \forall\, j=10,11,12,13,14.$$

7. Results and discussion

This section interprets the exact traveling-wave solutions obtained via the Sardar subequation method through the bifurcation structure of the reduced amplitude Eq (4.7), which arises from system (1.1) when we applied the transformation. The coefficients a and b are algebraic functions of the model parameters p_i, τ_i, w_i, and the wave number r_1.

The qualitative structure of the traveling-wave dynamics is controlled entirely by their signs. The associated planar system (5.1) is Hamiltonian, with first integral $H(z,w)=\frac{1}{2}w^2+\frac{1}{2}az^2+\frac{1}{4}bz^4$, and admits the trivial equilibrium $z=0$ together with the symmetric pair $z=\pm\sqrt{-a/b}$ when $-a/b>0$. As established in Section 5, the origin is a center for $a>0$ and a saddle for $a<0$, and the system undergoes a $\mathbb{Z}_2$-equivariant Hamiltonian pitchfork at $a=0$. Because the planar system is Hamiltonian, no equilibrium can be attracting, and the standard sub-/supercritical terminology of dissipative pitchforks does not apply here. Note that the values of parameters used in the figures are selected to meet the existence criteria of the associated exact solutions and to demonstrate representative wave profiles in the various bifurcation regimes revealed by the analytical analysis. Instead of reflecting a unique physical structure, these parameter sets serve as exemplary instances with well-defined analytical solutions and characteristic qualitative responses.

Formal and physically admissible solutions. Throughout this section, we distinguish between formal exact solutions and physically admissible traveling waves. A profile is regarded as a formal traveling-wave solution if it satisfies Eq (4.7) on its domain of definition. It is regarded as a regular physically admissible traveling wave only when it is real, globally defined on the considered real traveling coordinate, and bounded. Equation (6.4) provides the condition $b<0$ for a real amplitude coefficient μ_1, while the complementary branch $b>0$, $pq>0$ of Case I is real through the composite amplitude $\mu_1\sqrt{-pqr_1}$ (Section 6), but additional restrictions on p, q, and the denominators of the generalized Sardar functions are required to establish global reality and boundedness. Under these conditions, the regular sech_{pq} branch ($b>0$, $pq>0$) represents a bounded bright optical pulse and the $\tanh_{pq}$ branch ($b<0$, $pq>0$) can represent a bounded kink-type traveling wave, whereas branches whose generalized-function denominators vanish on the real axis are classified as singular formal solutions.

Phase-plane identity of the exact profiles. The classification of Subsection 5.3 assigns each Sardar profile a definite trajectory class in the reduced phase plane. Substituting $\Phi=\mu_1 U$ with $a=-r_1$ and $\mu_1^2=-2/b$ into the first integral (5.2) shows that every profile lies on a single explicit level set,

$$\mathcal{H}(z,w)=-\frac{r_0}{b},\tag{7.1}$$

so that its geometric character is fixed by (r_0,r_1,b). The profiles with $r_0=0$ lie on the level $\mathcal{H}=0$: For Case I with $b<0$, this is the level of the saddle at the origin, whose invariant manifolds are unbounded; for Case I with $b>0$, it is the figure-eight separatrix whose homoclinic loops carry the sech_{pq} soliton;

while for Case II, it is the level of the center, which is enclosed by no separatrix and is accompanied by two unbounded branches. The profiles with $r_0 = r_1^2/4$ lie on $\mathcal{H} = -r_1^2/(4b)$, which for Case III is the level of the saddles $E_\pm$ and carries the heteroclinic connection between them. The level set alone, however, does not determine admissibility: A profile is a regular traveling wave only if, in addition, the denominator of the corresponding generalized function has no real zero. Table 1 records the domain and pole structure of each profile together with the resulting classification. Only the sech_{pq} soliton of Case I ($b > 0$, $pq > 0$) and the $\tanh_{pq}$ kink of Case III ($b < 0$, $pq > 0$) satisfy all of these conditions. Table 1 summarizes the correspondence.

Scope of the bifurcation interpretation. Before discussing Figures 4–6 individually, we emphasize the following methodological point. The bifurcation diagram of Eq (5.1) (Figure 1) classifies the constant-amplitude equilibria of the reduced amplitude equation; the exact solutions plotted in Figures 4–6 are nonconstant trajectories of the same reduced system, expressed through the generalized functions csch_{pq} and $\tan_{pq}$ of the Sardar method. These solutions are therefore not plots of equilibrium branches; their behavior is interpreted via the class of phase-plane trajectory to which they correspond, within the parameter regime fixed by the signs of a and b. Consequently, the discussion below concerns the traveling-wave dynamics and not a full bifurcation analysis of the original fractional Fokas system.

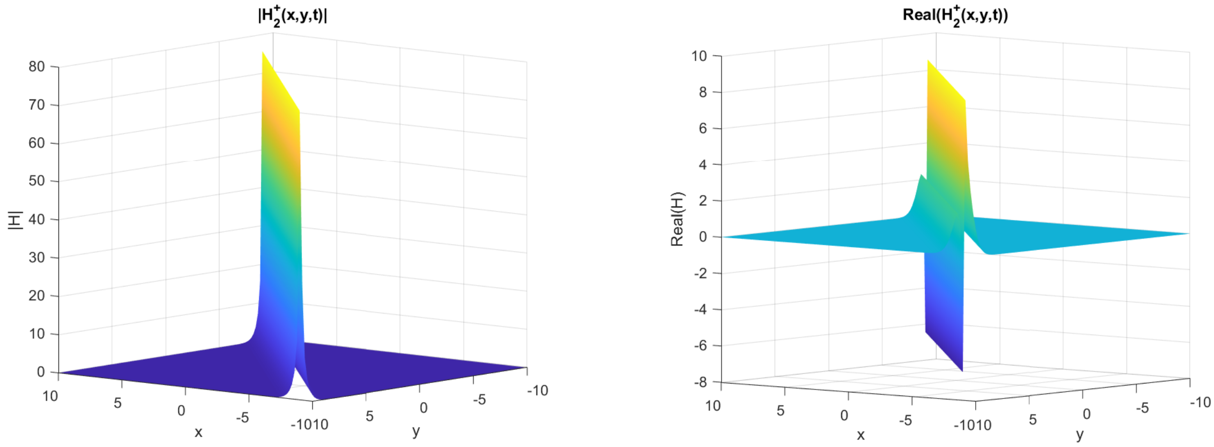

(a) Absolute value of the traveling wave solution $H_2^+(x, y, t)$ (Eq (6.6)).

(b) Traveling wave solution of the real part of $H_2^+(x, y, t)$ (Eq (6.6)).

Figure 4. Traveling wave solutions for the solution $H_2^+(x, y, t)$ (Eq (6.6)) under the values $p_1 = 0.5$, $p_2 = 0.1$, $p_3 = 1$, $p_4 = 0.5$, $\tau_2 = 1$, $\tau_3 = 1$, $w_1 = 1$, $w_2 = 1$, $w_3 = 0.5$, $r_1 = 2$, $p = 2$, $q = 2$, $\beta = 0.1$, $\delta = 1$, $-5 \le x, y \le 5$, $t = 1$. The profile is a csch_{pq} solution and is therefore singular: The spike is a pole, not a localized pulse. It is a formal traveling-wave solution lying on the unbounded level set $\mathcal{H} = 0$, the invariant manifolds of the saddle at the origin (no separatrix loop exists for $a < 0$, $b < 0$); the bounded member of Case I is the sech_{pq} soliton H_1^+ of Eq (6.5), realized on the complementary branch $b > 0$ ($\tau_2 < 0$) with $pq > 0$ (Subsection 5.3).

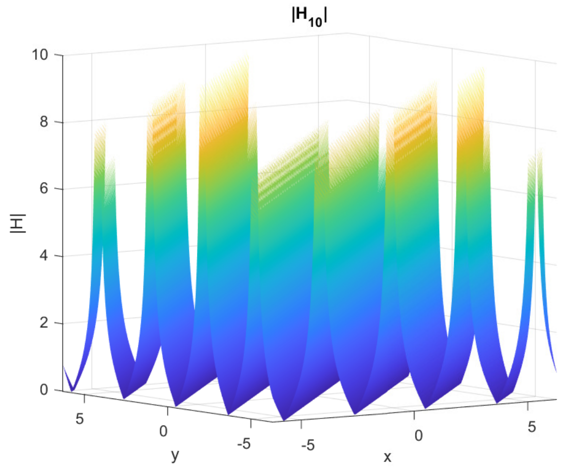

(a) Absolute value of the traveling wave solution $H_{10}^{+}(x, y, t)$ (Eq (6.8)).

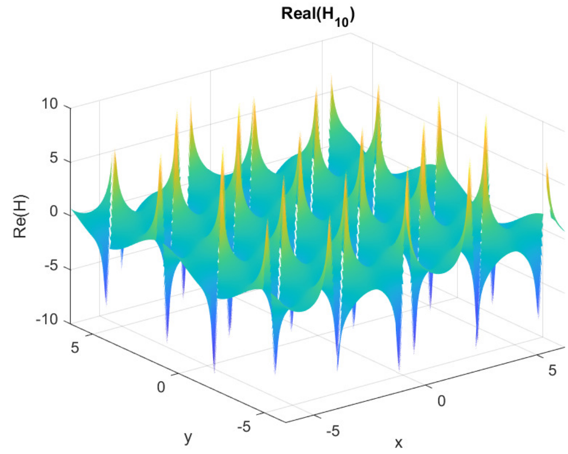

(b) Traveling wave solution of the real part of $H_{10}^{+}(x, y, t)$ (Eq (6.8)).

Figure 5. Traveling wave solutions for the solution $H_{10}^{+}(x, y, t)$ (Eq (6.8)) under the values $p_1 = 1$, $p_2 = 1$, $p_3 = 1$, $p_4 = 1$, $w_1 = 1$, $w_2 = 1$, $w_3 = 1$, $r_1 = 2$, $\tau_2 = 1$, $\tau_3 = 2$, $\beta = 1$, $\delta = 1$, $-2\pi \leq x, y \leq 2\pi$, $t = 0.5$. These values give $b = -1 < 0$, so the profile is real. It is a $\tan_{pq}$ solution and is periodic with poles; the repeated spikes are the poles, so the profile is a formal periodic solution and not a physically admissible optical wave-train.

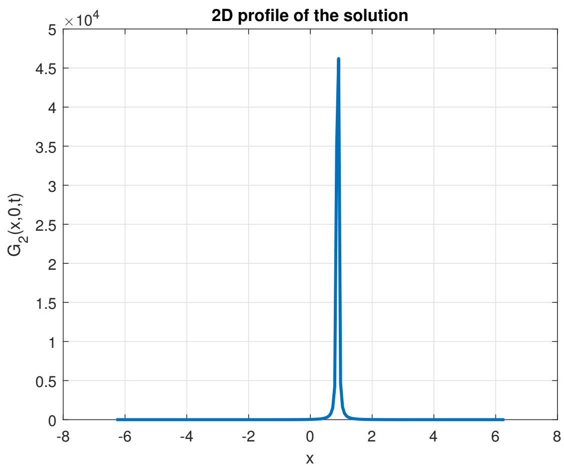

(a) Two-dimension graph for the traveling wave solution $G_2^{+}(x, y, t)$ (Eq (6.7)) when $t = 1$.

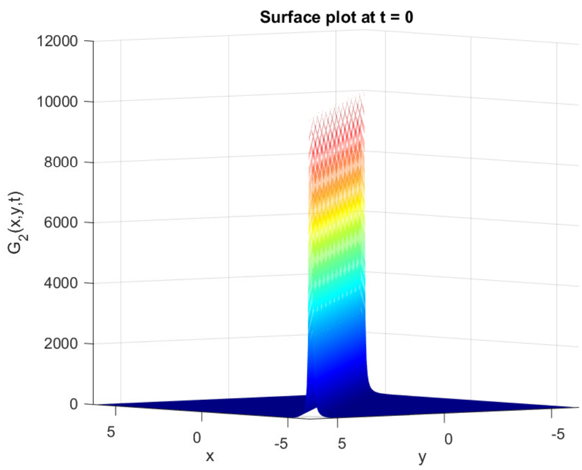

(b) Traveling wave solution of $G_2^{+}(x, y, t)$ (Eq (6.7)) when $t = 0$.

Figure 6. Traveling wave solutions for the solution $G_2^{+}(x, y, t)$ (Eq (6.7)) under the values $p_1 = 0.5$, $p_2 = 0.1$, $p_3 = 1$, $p_4 = 0.5$, $w_1 = 1$, $w_2 = 1$, $w_3 = 0.5$, $r_1 = 2$, $\tau_2 = 1$, $\tau_3 = 1$, $p = 2$, $q = 2$, $\beta = 0.1$, $\delta = 1$, $-2\pi \leq x, y \leq 2\pi$. The auxiliary field satisfies $G \propto \Phi^2$ with the negative prefactor $p_4\tau_1/(p_3\tau_2)$ on this branch ($\tau_1 < 0$, $\tau_2 > 0$) and is therefore non-positive; the panels display $|G_2^{+}|$. It inherits the pole of the corresponding H_2^{+} profile, so the peak is a singularity of the same formal solution.

The solution H_2^+ (Figure 4). For the parameter values listed in the caption of Figure 4, the balance condition $a = -r_1$ gives $a = -2$, and Eq (4.8) gives $b = -0.1$, so that μ_1 is real by Eq (6.4). Since $b < 0$ and $a < 0$ we have $-a/b < 0$, so the origin is the only equilibrium of Eq (5.1), and it is a saddle. By Eq (7.1) the profile H_2^+ (Case I, $r_0 = 0$) lies on the level $\mathcal{H} = 0$, that is, on the invariant manifolds of that saddle. The csch_{pq} factor is singular at the zero of its argument, and in the phase plane the corresponding trajectory escapes to infinity in a finite value of the traveling coordinate, consistent with the unbounded manifolds of the saddle. The large amplitudes visible in Figure 4 are the pole of csch_{pq}; they are not an instability of the fractional Fokas system, and neither are they a localized pulse. The physically admissible member of Case I is the sech_{pq} profile H_1^+ of Eq (6.5), realized on the complementary branch $b > 0$ ($\tau_2 < 0$) with $pq > 0$ (Subsection 5.3), where the level set $\mathcal{H} = 0$ is the figure-eight separatrix and the profile is its homoclinic loop; it describes a single localized optical pulse of finite energy propagating in a monomode fiber with fixed shape and speed.

The solution H_{10}^+ (Figure 5). For the parameter values of Figure 5 the balance condition again gives $a = -r_1 = -2$, while Eq (4.8) gives $b = -1 < 0$, so μ_1 is real and $-a/b = -2 < 0$: The origin is again the only equilibrium. The profile H_{10}^+ (Case IV, $r_0 = r_1^2/4$) lies, by Eq (7.1), on the level $\mathcal{H} = -r_1^2/(4b) = 1$, an unbounded level set. The $\tan_{pq}$ factor is periodic with poles, and the repeated spikes in Figure 5(a,b) are those poles. The profile is therefore a formal periodic solution of the reduced equation: It is exact and real, but its intensity diverges at a discrete set of points, and it does not describe a propagating optical wavetrain. For the present values $a < 0$ and $b < 0$, the origin is the only equilibrium and no closed orbit exists; bounded periodic profiles do exist in the reduced phase plane in the complementary regimes: for $a > 0$ and $b < 0$, the closed orbits surrounding the center inside the heteroclinic eye of Case III, and for $b > 0$ and $a < 0$, the closed orbits inside and around the figure-eight, but they are not among the Sardar-method solutions listed in Section 6; their construction is noted as an open problem in Section 8.

The auxiliary field G_2^+ (Figure 6). The auxiliary field G of the Fokas system is determined from H through the algebraic relation $G = (p_4\tau_1/p_3\tau_2)\,\Phi^2(\xi)$, so that G_j^+ inherits its qualitative shape from $|\Phi|^2$ of the corresponding H_j^+. Figure 6 displays G_2^+; the two-dimensional slice at fixed t in Figure 6(a) and the surface plot in Figure 6(b) both exhibit the sharp peak expected from the csch_{pq} singularity, now squared; since the prefactor $p_4\tau_1/(p_3\tau_2)$ is negative on this branch ($\tau_1 < 0$, $\tau_2 > 0$), G_2^+ is nonpositive rather than nonnegative. As a consequence, G_2^+ does not change sign and $|G_2^+|$ attains substantially larger amplitudes than $|H_2^+|$ on the same domain, but the location of its singular structure coincides exactly with that of H_2^+, in agreement with the common dependence on the traveling coordinate ξ. The peak is therefore a pole of the same formal solution, and G_2^+ is admissible only in the same sense as H_2^+; the bounded counterpart is G_1^+, realized on the soliton branch $b > 0$, where the prefactor $p_4\tau_1/(p_3\tau_2)$ is positive ($\tau_1 < 0$, $\tau_2 < 0$) so that G_1^+ is a nonnegative localized hump inheriting its localization from the sech_{pq} soliton.

Role of the fractional parameters. A structural feature worth noting is that the fractional parameters β and δ enter the reduction only through the traveling coordinate $\xi = \tau_1 x + \tau_2 y + \tau_3 \Gamma(\beta+1) t^\delta/\delta$ and the phase, and do not enter the reduced coefficients a and b. As established in Remark 2.1, this is a consequence of the local character of the D-truncated derivative, which acts as a weighted classical derivative and is independent of the truncation index k; the same holds for the M-truncated, conformable, and β-derivatives. We therefore do not claim that the reduced dynamics are fractional. What δ and β control is the realization of a given profile in (x, y, t): through ξ the profile is transported along t^δ rather than t, so that its propagation is non-uniform in time, while its shape and its phase-plane class are unchanged. In this precise and limited sense the D-truncated operator alters where and when a profile appears, and leaves the bifurcation diagram of Eq (5.1) invariant. Stability of these profiles within the full fractional Fokas system, including the effect of β and δ on long-time dynamics, is a separate question that lies outside the scope of the present traveling-wave reduction.

8. Conclusions

The traveling-wave reduction of the Fokas system with the D-truncated fractional derivative yields Eq (4.7). Because the D-truncated operator is local and independent of its truncation index, the reduced equation carries no dependence on k, δ, or β: The fractional orders enter only through the traveling coordinate and the phase, so they determine where and when a given profile is realized in (x, y, t), but not which profiles exist. We state this plainly as a property of the reduction rather than as a feature of the model, and it is shared by every local truncated operator in current use. The exact Sardar-subequation profiles are classified according to the first integral of the reduced Hamiltonian equation. Although $b < 0$ is necessary for the amplitude coefficient μ_1 to be real, real bounded profiles arise on both branches of the sign of b, since for $b > 0$ the product of the imaginary μ_1 with the imaginary Case I amplitude factor is real; the complete reality and boundedness of a profile additionally depend on the parameters p and q and on the absence of real zeros in the denominators of the corresponding generalized Sardar functions. Consequently, the exact expressions are divided into regular bounded traveling waves and formal singular solutions. In particular, the Case I sech_{pq} branch ($b > 0$, $pq > 0$) provides a bright optical soliton, and the Case III $\tanh_{pq}$ branch ($b < 0$, $pq > 0$) can provide a regular bounded kink-type wave under appropriate parameter conditions, whereas profiles whose generalized-function denominators vanish on the real traveling coordinate are singular and should not be interpreted as physically admissible optical pulses.

The reduced system is Hamiltonian and $\mathbb{Z}_2$-equivariant, and its symmetric branch loses stability through a Hamiltonian pitchfork at $a = 0$. The bifurcation point is degenerate, with a nilpotent linearization that obstructs standard branch-point continuation; the obstruction is removed by enforcing symmetry on the continued solution while leaving the critical eigenvector free, and the resulting numerical locus $\{a = 0\}$ agrees with the analytical prediction to machine precision. As the locus is available in closed form, this computation is a verification of the equivariant defining system rather than a result about the Fokas system; its interest lies in confirming the formulation before it is applied where no closed form exists, for instance, to equivariant delay equations. Two questions remain open at the boundary of the reduction. First, the reduced phase plane supports bounded profiles that the Sardar-method solutions listed here do not realize: the closed periodic orbits surrounding the centers–the cnoidal wave-trains, available for the Fokas system through the Jacobi elliptic constructions of [15] but not through the Sardar ansatz used here. Their explicit construction within the present phase-plane framework as (x, y, t) profiles would complete the catalogue of physically admissible traveling waves. Second, the independence of the reduced diagram from δ and β is a statement about the traveling-wave reduction, not about stability; whether the profiles retain their character under the full fractional flow is a separate question, addressable only outside the traveling-wave assumption. Extending the current methodology to more general fractional operators and higher-dimensional nonlinear evolution equations that arise in optical physics and wave propagation is another potential area.

Author contributions

Both authors contributed to the conceptualization of the study, the analytical derivations, and the preparation and revision of the manuscript. Both authors have read and approved the final version of the manuscript for publication.

Use of Generative-AI tools declaration

The authors declare they have not used Artificial Intelligence (AI) tools in the creation of this article.

Funding

This work was supported and funded by the Deanship of Scientific Research at Imam Mohammad Ibn Saud Islamic University (IMSIU) (grant number IMSIU-DDRSP2602).

Conflict of interest

The authors declare no conflicts of interest.

References

1. G. B. Whitham, *Linear and nonlinear waves*, John Wiley & Sons, 2011.
2. J. D. Murray, Reaction diffusion, chemotaxis, and nonlocal mechanisms, In: *Mathematical biology: I. An introduction*, New York: Springer, 2002, 395–417. https://doi.org/10.1007/978-0-387-22437-4_11
3. P. G. Drazin, R. S. Johnson, *Solitons: An introduction*, Cambridge University Press, 1989.
4. U. Akpan, L. Akinyemi, D. Ntiamoah, A. Houwe, S. Abbagari, Generalized stochastic Korteweg-de Vries equations, their Painlevé integrability, N-soliton and other solutions, *Int. J. Geom. Methods Mod. Phys.*, **21** (2024), 2450128. https://doi.org/10.1142/S0219887824501287
5. A. Houwe, S. Abbagari, L. Akinyemi, A. S. M. Metwally, S. Y. Doka, Wave patterns of the coupled nonlinear Schrödinger equations in photonic crystal fibers with four-wave mixing, *Phys. Scr.*, **99** (2024), 115223. https://doi.org/10.1088/1402-4896/ad7fa6
6. W. W. Mohammed, C. Cesarano, F. M. Al-Askar, Solutions to the (4+1)-dimensional time-fractional Fokas equation with M-truncated derivative, *Mathematics*, **11** (2023), 194. https://doi.org/10.3390/math11010194
7. W. W. Mohammed, C. Cesarano, A. A. Elmandouh, I. Alqsair, R. Sidaoui, H. W. Alshammari, Abundant optical soliton solutions for the stochastic fractional Fokas system using bifurcation analysis, *Phys. Scr.*, **99** (2024), 045233. https://doi.org/10.1088/1402-4896/ad30fd
8. F. M. Al-Askar, Optical solitons for the Fokas-Lenells equation with beta and M-truncated derivatives, *J. Funct. Spaces*, **2023** (2023), 8883811. https://doi.org/10.1155/2023/8883811

9. H. Bulut, U. Demirbilek, E. Çelik, Dynamical soliton solutions of (2+1)-dimensional paraxial wave and (4+1)-dimensional Fokas wave equations with truncated M-fractional derivative using an efficient technique, *J. Math.*, **2025** (2025), 6659392. https://doi.org/10.1155/jom/6659392

10. T. Rasool, R. Hussain, H. Rezazadeh, A. Ali, U. Demirbilek, Novel soliton structures of truncated M-fractional (4+1)-dim Fokas wave model, *Nonlinear Eng.*, **12** (2023), 20220292. https://doi.org/10.1515/nleng-2022-0292

11. J. G. Rao, D. Mihalache, Y. Cheng, J. S. He, Lump-soliton solutions to the Fokas system, *Phys. Lett. A*, **383** (2019), 1138–1142. https://doi.org/10.1016/j.physleta.2018.12.045

12. M. F. Alotaibi, N. Raza, M. H. Rafiq, A. Soltani, New solitary waves, bifurcation and chaotic patterns of Fokas system arising in monomode fiber communication system, *Alex. Eng. J.*, **67** (2023), 583–595. https://doi.org/10.1016/j.aej.2022.12.069

13. M. A. S. Murad, F. K. Hamasalh, H. F. Ismael, Optical soliton solutions for time-fractional Fokas system in optical fiber by new Kudryashov approach, *Optik*, **280** (2023), 170784. https://doi.org/10.1016/j.ijleo.2023.170784

14. N. Iqbal, M. S. Aldhabani, N. Alam, A. E. Hamza, W. W. Mohammed, A. A. Hamoud, Fractional dynamics and optical soliton propagation in mono-mode fibers via the Fokas system, *Sci. Rep.*, **16** (2026), 9280. https://doi.org/10.1038/s41598-026-39656-4

15. W. W. Mohammed, C. Cesarano, E. M. Elsayed, F. M. Al-Askar, The analytical fractional solutions for coupled Fokas system in fiber optics using different methods, *Fractal Fract.*, **7** (2023), 1–13. https://doi.org/10.3390/fractalfract7070556

16. A. S. Fokas, On the simplest integrable equation in 2+1, *Inverse Problems*, **10** (1994), L19–L22. https://doi.org/10.1088/0266-5611/10/2/002

17. A. S. Fokas, On a class of physically important integrable equations, *Phys. D Nonlinear Phenom.*, **87** (1995), 145–150. https://doi.org/10.1016/0167-2789(95)00133-O

18. M. Golubitsky, I. Stewart, *The symmetry perspective: From equilibrium to chaos in phase space and physical space*, Basel: Birkhäuser, 2002. https://doi.org/10.1007/978-3-0348-8167-8

19. A. A. Alawfi, *Symmetry breaking in a delay differential equation modelling auditory streaming*, Ph.D. Thesis, University of Exeter, 2024.

20. C. Wulff, A. Schebesch, Numerical continuation of symmetric periodic orbits, *SIAM J. Appl. Dyn. Syst.*, **5** (2006), 435–475. https://doi.org/10.1137/050637170

21. M. Golubitsky, I. Stewart, D. G. Schaeffer, *Singularities and Groups in bifurcation theory: Volume II*, New York: Springer, 1988. https://doi.org/10.1007/978-1-4612-4574-2

22. A. Vanderbauwhede, *Local bifurcation and symmetry*, Boston: Pitman Advanced Publishing Program, 1982.

23. B. Werner, A. Spence, The computation of symmetry-breaking bifurcation points, *SIAM J. Numer. Anal.*, **21** (1984), 388–399. https://doi.org/10.1137/0721029

24. W. J. F. Govaerts, *Numerical methods for bifurcations of dynamical equilibria*, Philadelphia: SIAM, 2000. https://doi.org/10.1137/1.9780898719543

25. A. Dhooge, W. Govaerts, Y. A. Kuznetsov, MATCONT: A MATLAB package for numerical bifurcation analysis of ODEs, *ACM Trans. Math. Softw. (TOMS)*, **29** (2003), 141–164. https://doi.org/10.1145/779359.779362
26. H. Dankowicz, F. Schilder, *Recipes for continuation*, Philadelphia: SIAM, 2013. https://doi.org/10.1137/1.9781611972573
27. K. Engelborghs, T. Luzyanina, D. Roose, Numerical bifurcation analysis of delay differential equations using DDE-BIFTOOL, *ACM Trans. Math. Softw. (TOMS)*, **28** (2002), 1–21. https://doi.org/10.1145/513001.513002
28. J. Sieber, K. Engelborghs, T. Luzyanina, G. Samaey, D. Roose, *DDE-BIFTOOL v. 3.1.1 Manual–Bifurcation analysis of delay differential equations*, 2014, arXiv: 1406.7144.